

Model-based Learning for Quantitative Susceptibility Mapping

Juan Liu^{1,2} and Kevin M. Koch^{1,2,3}

¹ Center for Imaging Research, Medical College of Wisconsin, Milwaukee, WI, USA

² Department of Biomedical Engineering, Marquette University and Medical College of Wisconsin, Milwaukee, WI, USA

³ Department of Radiology, Medical College of Wisconsin, Milwaukee, WI, USA
juan.liu@marquette.edu

Abstract. Quantitative susceptibility mapping (QSM) is a magnetic resonance imaging (MRI) technique that estimates magnetic susceptibility of tissue from Larmor frequency offset measurements. The generation of QSM requires solving a challenging ill-posed field-to-source inversion problem. Inaccurate field-to-source inversion often causes large susceptibility estimation errors that appear as streaking artifacts in the QSM, especially in massive hemorrhagic regions. Recently, several deep learning (DL) QSM techniques have been proposed and demonstrated impressive performance. Due to the inherent non-existent ground-truth QSM references, these DL techniques used either calculation of susceptibility through multiple orientation sampling (COSMOS) maps or synthetic data for network training. Therefore, they were constrained by the availability and accuracy of COSMOS maps, or suffered from performance drop when the training and testing domains were different. To address these limitations, we present a model-based DL method, denoted as uQSM. Without accessing to QSM labels, uQSM is trained using the well-established physical model. When evaluating on multi-orientation QSM datasets, uQSM achieves higher levels of quantitative accuracy compared to TKD, TV-FANSI, MEDI, and DIP approaches. When qualitatively evaluated on single-orientation datasets, uQSM outperforms other methods and reconstructed high quality QSM.

Keywords: Quantitative susceptibility mapping · Self-supervised learning · Dipole inversion.

1 Introduction

Quantitative susceptibility mapping (QSM) can estimate tissue magnetic susceptibility values from magnetic resonance imaging (MRI) Larmor frequency sensitive phase images [31]. Biological tissue magnetism can provide useful diagnostic image contrast and be used to quantify biomarkers including iron, calcium, and gadolinium [31]. To date, all QSM methods rely on a dipolar convolution that relates susceptibility sources to induced Larmor frequency offsets [25,20], which is expressed in the k-space as bellow.

$$B(\mathbf{k}) = X(\mathbf{k}) \cdot D(\mathbf{k}); D(\mathbf{k}) = \frac{1}{3} - \frac{k_z^2}{k_x^2 + k_y^2 + k_z^2} \quad (1)$$

where $B(\mathbf{k})$ is the susceptibility induced magnetic perturbation along the main magnetic field direction, $X(\mathbf{k})$ is the susceptibility distribution χ in the k space, $D(\mathbf{k})$ is the dipole kernel. While the forward relationship of this model (source to field) is well-established and can be efficiently computed using Fast-Fourier-Transform (FFT), the k -space singularity in the dipole kernel results in an ill-conditioned relationship in the field-to-source inversion.

Calculation of susceptibility through multiple orientation sampling (COSMOS) [18] remains the empirical gold-standard of QSM, as the additional field data sufficiently improves the conditioning of the inversion algorithm. Since it is time-consuming and clinically infeasible to acquire multi-orientation data, single-orientation QSM is preferred which is computed by either thresholding of the convolution operator [27,32,9] or use of more sophisticated regularization methods [6,24,17,2]. In single-orientation QSM, inaccurate field-to-source inversion often causes large susceptibility estimation errors that appear as streaking artifacts in the QSM, especially in massive hemorrhagic regions.

Recently, several deep learning (DL) approaches have been proposed to solve for the QSM dipole inversion. QSMnet [34] used COSMOS results as QSM labels for training, which reconstructed COSMOS-like QSM estimates no matter the head orientations. DeepQSM [3] used synthetic susceptibility maps simulated using basic 3D geometric shapes and the forward dipole model to generate synthetic training data. QSMGAN [5] adopted COSMOS maps as QSM labels and refined the network using the Wasserstein Generative Adversarial Networks (WGAN) [7,1]. QSMnet+ [12] employed data augmentation approaches to increase the range of susceptibility, which improved the linearity of susceptibility measurement in clinical situations.

Though these DL techniques have exhibited impressive results, there were several limitations. These methods are supervised and data-driven which require QSM labels for network training. Unfortunately, QSM has the inherent non-existent ‘ground-truth’. Therefore, these methods used either COSMOS data or synthetic data for network training. However, acquiring a large number of COSMOS data is not only expensive but also time consuming. Moreover, COSMOS neglects tissue susceptibility anisotropy [15] and contains errors from background field removal and image registration procedures, which compromises COSMOS map as a QSM label. Though synthetic data provides a reliable and cost-effective way for training, the generalization capability needs to be addressed since the domain gap between the synthetic training data and real data often causes performance degradation and susceptibility quantification errors.

Here, we propose a model-based learning method without the need of QSM labels for QSM dipole inversion, denoted as uQSM, to overcome these limitations. Quantitative evaluation is performed on multi-orientation datasets in comparison to TKD [27], TV-FANSI [21], MEDI [16], and deep image prior (DIP)[30], with

COSMOS result as a reference. In addition, qualitative evaluation is performed on single-orientation datasets.

2 Method

uQSM adopted a 3D convolutional neural network with an encoder-decoder architecture as shown in Fig.1.

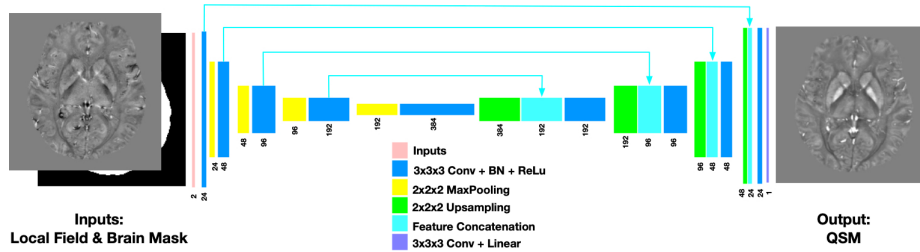


Fig. 1. Neural network architecture of uQSM. It has an encoder-decoder structure with 9 convolutional layers (kernel size 3x3x3, same padding), 9 batch normalization layers, 9 ReLU layers, 4 max pooling layers (pooling size 2x2x2, strides 2x2x2), 4 nearest-neighbor upsampling layers (size 2x2x2), 4 feature concatenations, and 1 convolutional layer (kernel size 3x3x3, linear activation).

The network took two inputs, a local field measurement f and a brain mask m , and one output, a susceptibility map χ . Upsampling layers were used in the decoding path in stead of deconvolutional layers to address the checkboard artifacts [22] in the reconstructed QSM.

The loss function incorporated the model-based data consistency loss L_χ .

$$L_\chi = \|Wm(e^{jd*\chi} - e^{jf})\|_2 \quad (2)$$

where W serves as a data-weighting factor which can be the magnitude image or noise weight matrix, d is the dipole kernel, $*$ is the convolution operator. Since noise is unknown and spatially variant in the local field measurements, the nonlinear dipole convolution data consistency loss was used in the loss function to get more robust QSM estimates as conventional QSM methods [19,23]. The dipole convolution was computed in the k-space using FFT.

For normalization, the mean and standard deviation were calculated in the local fields. Then, the input local maps were normalized to have a mean of 0 and a standard deviation of 1. Since the susceptibility maps were unknown, we used $3d * \chi$ to be consistent with f , which can make the susceptibility outputs close to being standard normalized.

$$L_{TV} = \|G_x(\chi)\|_1 + \|G_y(\chi)\|_1 + \|G_z(\chi)\|_1 \quad (3)$$

In addition, a total variation (TV) loss L_{TV} was included to serve as a regularization term to preserve important details such as edges whilst removing

unwanted noise in the reconstructed susceptibility maps. In L_{TV} , G_x , G_y , G_z are gradient operators in x, y, z directions.

$$L_{Total} = L_{\chi} + \lambda L_{TV} \quad (4)$$

The loss function is the weighted sum of the data consistency loss L_{χ} and the total variation loss L_{TV} .

3 Experiments

Multi-orientation QSM Data 9 QSM datasets were acquired using 5 head orientations and a 3D single-echo GRE scan with isotropic voxel size $1.0 \times 1.0 \times 1.0 \text{ mm}^3$ on 3T MRI scanners. QSM data processing was implemented as following, offline GRAPPA [8] reconstruction to get magnitude and phase images from saved k-space data, coil combination using sensitivities estimated with ESPiRiT [29], BET (FSL, FMRIB, Oxford, UK) [28] for brain extraction, Laplacian method [14] for phase unwrapping, and RESHARP [33] with spherical mean radius 4mm for background field removal. COSMOS results were calculated using the 5 head orientation data which were registered by FLIRT (FSL, FMRIB, Oxford, UK) [10,11]. In addition, QSM estimates at the normal head position were generated using the TKD, TV-FANSI, and MEDI algorithms.

For uQSM, leave-one-out cross validation was used. For each dataset, total 40 scans from other 8 datasets were used for training. uQSM was trained using patch-based neural network with patch size $96 \times 96 \times 96$. The RESHARP local field and brain mask patches with patch size $96 \times 96 \times 96$ were cropped with an overlapping scheme of 16.6 percent overlap between adjacent patches. These patch pairs were used for training and validation with split ratio 9:1. The magnitude images were scaled between 0 to 1 and used as the weighting factor W , λ was set 0.001. The Adam optimizer [13] was used for the model training. The initial learning rate was set as 0.0001, with exponentially decay at every 100 steps. One NVIDIA GPU Tesla k40 was used for training with batch size 4. The model was trained and evaluated using Keras with Tensorflow as a backend. After training, the full local field and brain mask from the leave-one dataset were fed to the trained model to get the QSM estimates.

In addition, we used DIP to get the QSM images. DIP used the same neural network architecture and loss function described above. DIP was performed on each individual dataset using full neural network. To avoid overfitting which can introduce artifacts in the reconstructed QSM images, DIP was stopped after 200 iterations to get QSM results.

The QSM of uQSM, TKD, TV-FANSI, MEDI, and DIP were compared with respect to the COSMOS maps using quantitative metrics, peak signal-to-noise ratio (pSNR), normalized root mean squared error (NRMSE), high frequency error norm (HFEN), and structure similarity (SSIM) index.

Single-orientation QSM Data 150 QSM datasets were collected on a 3T MRI scanner (GE Healthcare MR750) from a commercially available susceptibility weighted software application (SWAN, GE Healthcare). The data acquisition

parameters were as follows: in-plane data matrix 320x256, field of view 24 cm, voxel size 0.5x0.5x2.0 mm³, 4 echo times [10.4, 17.4, 24.4, 31.4] ms, repetition time 58.6 ms, autocalibrated parallel imaging factors 3x1, and total acquisition time 4 minutes.

Complex multi-echo images were reconstructed from raw k-space data using customized code. The brain masks were obtained using the SPM tool [4]. After background field removal using the RESHARP with spherical mean radius 4mm, susceptibility inversion was performed using TKD, TV-FANSI, and MEDI. In addition, we used DIP to get the QSM images. DIP was performed for each individual dataset and early stopped after 200 iterations.

For uQSM training, 10449 patch pairs of local field maps and brain masks with patch size 128x128x64 were extracted from 100 QSM datasets. The average of multi-echo magnitude images was scaled between 0 to 1 and used as the weighting factor W . In the loss function, λ was set 0.0 since the data had high signal-to-noise ratio. The Adam optimizer was used with an initial learning rate 0.0001, which exponentially decayed at every 100 steps. One NVIDIA GPU Tesla k40 was used for training with batch size 2. After training, the trained DL model took full local fields and brain masks to get the QSM estimates.

4 Experimental Results

Table 1. Means and standard deviations of quantitative performance metrics of 5 reconstructed QSM images with COSMOS as a reference on 9 multi-orientation datasets.

	pSNR (dB)	NRMSE (%)	HFEN (%)	SSIM (0-1)
TKD	43.4 ± 0.5	91.4 ± 6.7	72.9 ± 6.6	0.831 ± 0.016
TV-FANSI	41.5 ± 0.6	80.0 ± 5.0	73.6 ± 6.2	0.869 ± 0.019
MEDI	41.5 ± 0.6	113.8 ± 7.6	100.4 ± 9.1	0.902±0.016
DIP	44.0 ± 0.8	85.5 ± 6.7	65.7 ± 4.5	0.859 ± 0.020
uQSM	45.6±0.4	71.4±5.0	62.8±5.0	0.890 ± 0.015

Multi-orientation QSM Data Table.1 summarized quantitative metrics of 5 reconstruction methods on 9 multi-orientation datasets with COSMOS map as a reference. Compared to TKD, TV-FANSI, MEDI, and DIP, uQSM results achieved the best metric scores in pSNR, RMSE, and HFEN, and second in SSIM. Fig.2 compared QSM images from a representative dataset in three planes. Streaking artifacts were observed in the sagittal planes of TKD, TV-FANSI, and MEDI results (a-c, iii, black solid arrows). TV-FANSI and MEDI maps showed substantial blurring due to their use of spatial regularization. DIP results displayed good image quality. uQSM demonstrated superior image sharpness and invisible image artifacts. Compared with uQSM, COSMOS results displayed conspicuity loss due to image registration errors (e-f, i, black dash arrows).

Single-orientation QSM Data Fig.3 displayed QSM images from a single-orientation dataset. TKD, MEDI results had black shading artifacts in the axial plane, and streaking artifacts in coronal and sagittal planes. MEDI and TV-FANSI images showed oversmoothing and lost image sharpness. DIP results

showed high quality but subtle image artifacts. Visual comparison demonstrated that uQSM outperformed other methods and produced better QSM images.

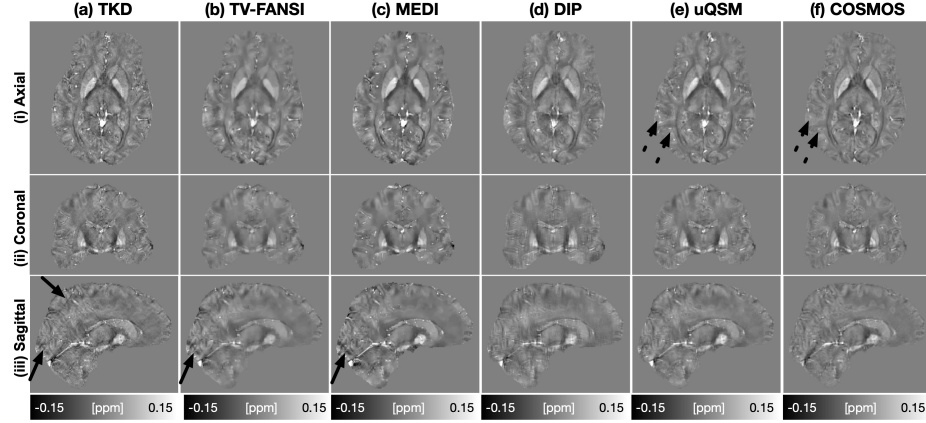


Fig. 2. Comparison of QSM of a multi-orientation data. TKD (a), TV-FANSI (b) and MEDI (c) maps showed oversmoothing and/or streaking artifacts. The uQSM (e) maps well preserved image details and showed invisible artifacts.

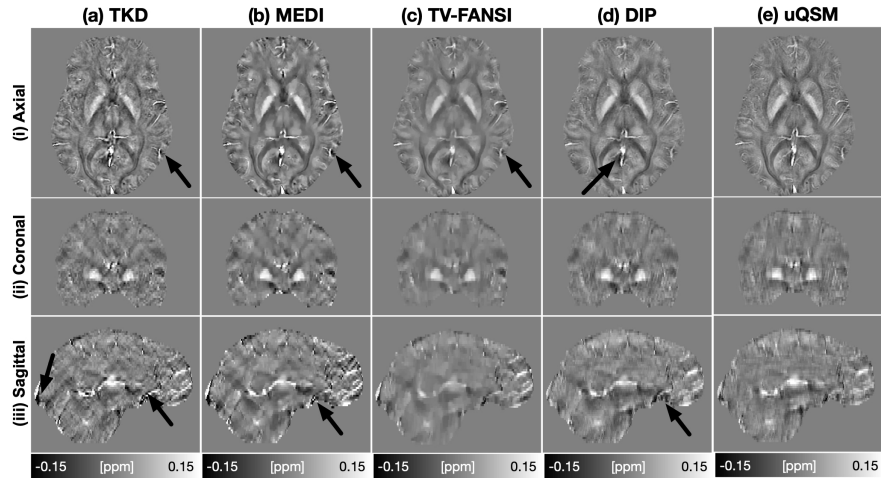


Fig. 3. Comparison of QSM of a single-orientation dataset. TDK (a), MEDI (b), and DIP (d) results showed black shading artifacts in the axial plane and streaking artifacts in the sagittal plane. MEDI (b) and TV-FANSI (c) results suffered from oversmoothing. uQSM (e) images had high-quality with clear details and invisible artifacts.

Deconvolution and Checkboard Artifacts In uQSM, we used upsampling layers rather than deconvolutional layers to reduce the checkerboard artifacts [22] in QSM results. Here we trained two networks on the single-orientation datasets, one with upsampling and the other with deconvolution in the decoding path. Fig.4 compared QSM images of 2 single-orientation datasets reconstructed using deconvolution-based network and upsampling-based network.

Deconvolution-based network produced QSM with checkboard artifacts in the zoom-in axial plane (a, ii, black arrows).

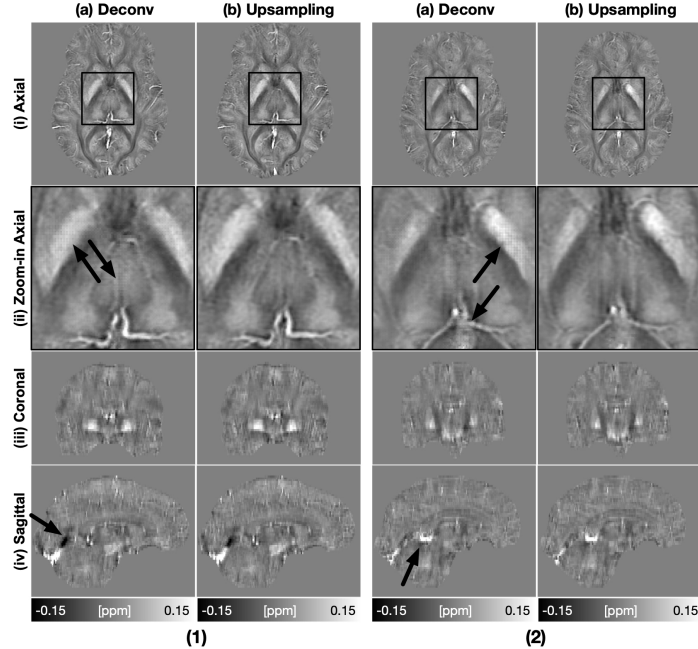


Fig. 4. Comparison of QSM results of 2 single-orientation datasets. uQSM using deconvolution (a) showed checkboard artifacts in zoom-in axial plane (a, ii, black arrows).

Effects of L_{TV} and Data Consistency Losses We used the multi-orientation datasets to investigate the effects of L_{TV} and three data consistency losses - (1) linear dipole inversion (LDI), $L_{LDI} = \|m(d * \chi - y)\|_2$, (2) weighted linear dipole inversion (WLDI), $L_{WLDI} = \|Wm(e^{id*\chi} - e^{iy})\|_2$, (3) weighted nonlinear dipole inversion (NDI), $L_{NDI} = \|Wm(d * \chi - y)\|_2$.

Table 2. Means and standard deviations of quantitative performance metrics of uQSM using different loss function on 9 multi-orientation datasets.

	pSNR (dB)	NRMSE (%)	HFEN (%)	SSIM (0-1)
L_{NDI}	43.8 ± 0.5	87.4 ± 6.8	70.5 ± 5.7	0.848 ± 0.022
$L_{LDI} + \lambda L_{TV}$	44.1 ± 0.5	84.9 ± 5.9	73.4 ± 5.7	0.879 ± 0.013
$L_{LWLDI} + \lambda L_{TV}$	45.0 ± 0.5	75.9 ± 5.4	67.1 ± 5.5	0.888 ± 0.015
$L_{NDI} + \lambda L_{TV}$	45.6 ± 0.4	71.4 ± 5.0	62.8 ± 5.0	0.890 ± 0.015

Table.2 summarized quantitative metrics on 9 multi-orientation datasets with COSMOS map as a reference. uQSM using $L_{NDI} + \lambda L_{TV}$ achieved the best metric scores. Fig.5 displayed QSM images. Without L_{TV} , the QSM showed high level of noise (a). Using L_{LDI} and L_{WLDI} as data consistency loss, the QSM estimates displayed black shading artifacts (b-c, i-iii, black arrows), while L_{NDI} was capable of suppressing these artifacts.

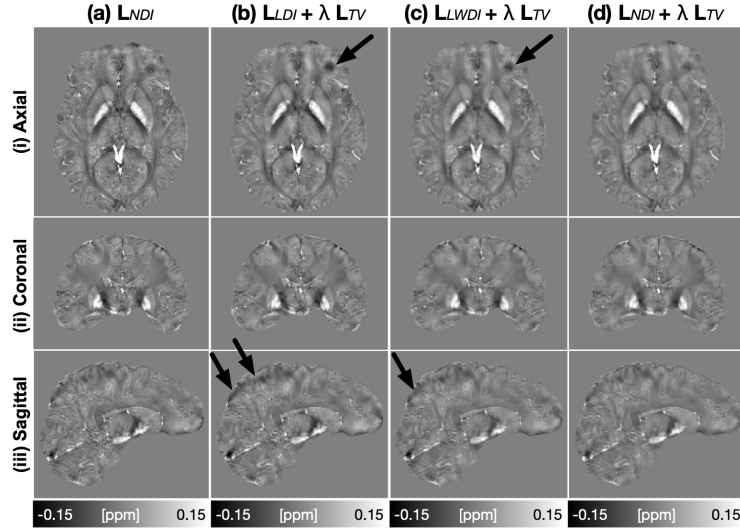


Fig. 5. Comparison of uQSM results using different loss functions of one multi-orientation datasets.

5 Discussion and Conclusion

In this work, a model-based DL method for QSM dipole deconvolution was proposed. Without accessing to QSM labels during training, uQSM learned to perform dipole inversion through the physical model.

From quantitative evaluation on multi-orientation QSM datasets, uQSM outperformed TKD, TV-FANSI, MEDI, and DIP in pSNR, RMSE, and HFEN, with COSMOS map as a reference. The visual assessment demonstrated that uQSM preserved image details well and showed invisible image artifacts. When using single-orientation datasets for qualitative assessment, uQSM results showed better image quality than conventional non-DL methods and DIP. Though DIP is unsupervised and does not require training data for prior training, it needs long iteration times for each dataset and early-stopping to avoid overfitting. In addition, the upsampling used in uQSM network can avoid the checkerboard artifacts in the QSM estimates. L_{TV} enable to denosing the QSM outputs and preserve the edge information. L_{NDI} as data consistency loss can improve the image quality of uQSM than L_{LDI} and L_{LWDI} .

Future work can apply more sophisticated models [26] in uQSM. In addition, uQSM is still affected by the performance of background field removal methods. It is necessary to investigate the effects of background field removal on susceptibility quantification or perform DL-based single-step QSM reconstruction.

Acknowledgement

We thank Professor Jongho Lee for sharing the multi-orientation QSM datasets.

References

1. Arjovsky, M., Chintala, S., Bottou, L.: Wasserstein generative adversarial networks. In: International conference on machine learning. pp. 214–223 (2017)
2. Bilgic, B., Chatnuntawech, I., Fan, A.P., et al: Fast image reconstruction with L2-regularization. *Journal of Magnetic Resonance Imaging* **40**(1), 181–191 (2014)
3. Bollmann, S., Rasmussen, K.G.B., Kristensen, M., et al: DeepQSM-using deep learning to solve the dipole inversion for quantitative susceptibility mapping. *NeuroImage* **195**, 373–383 (2019)
4. Brett, M., Anton, J.L., Valabregue, R., et al: Region of interest analysis using an SPM toolbox. In: 8th International Conference on Functional Mapping of the Human Brain. p. 497. Sendai (2002)
5. Chen, Y., Jakary, A., Avadiappan, S., et al: QSMGAN: Improved quantitative susceptibility mapping using 3d generative adversarial networks with increased receptive field. *NeuroImage* p. 116389 (2019)
6. De Rochefort, L., Brown, R., Prince, M.R., et al: Quantitative MR susceptibility mapping using piece-wise constant regularized inversion of the magnetic field. *Magnetic Resonance in Medicine* **60**(4), 1003–1009 (2008)
7. Goodfellow, I., Pouget-Abadie, J., Mirza, M., et al: Generative adversarial nets. In: Advances in neural information processing systems. pp. 2672–2680 (2014)
8. Griswold, M.A., Jakob, P.M., Heidemann, R.M., Nittka, M., Jellus, V., Wang, J., Kiefer, B., Haase, A.: Generalized autocalibrating partially parallel acquisitions (GRAPPA). *Magnetic Resonance in Medicine* **47**(6), 1202–1210 (2002)
9. Haacke, E., Tang, J., Neelavalli, J., et al: Susceptibility mapping as a means to visualize veins and quantify oxygen saturation. *Journal of Magnetic Resonance Imaging* **32**(3), 663–676 (2010)
10. Jenkinson, M., Bannister, P., Brady, M., et al: Improved optimization for the robust and accurate linear registration and motion correction of brain images. *NeuroImage* **17**(2), 825–841 (2002)
11. Jenkinson, M., Smith, S.: A global optimisation method for robust affine registration of brain images. *Medical image analysis* **5**(2), 143–156 (2001)
12. Jung, W., Yoon, J., Ji, S., et al: Exploring linearity of deep neural network trained QSM: QSMnet+. *NeuroImage* **211**, 116619 (2020)
13. Kingma, D.P., Ba, J.: Adam: A method for stochastic optimization. *arXiv* (2014)
14. Li, W., Wu, B., Liu, C.: Quantitative susceptibility mapping of human brain reflects spatial variation in tissue composition. *NeuroImage* **55**(4), 1645–1656 (2011)
15. Liu, C.: Susceptibility tensor imaging. *Magnetic Resonance in Medicine* **63**(6), 1471–1477 (2010)
16. Liu, J., Liu, T., de Rochefort, L., et al: Morphology enabled dipole inversion for quantitative susceptibility mapping using structural consistency between the magnitude image and the susceptibility map. *NeuroImage* **59**(3), 2560–2568 (2012)
17. Liu, T., Liu, J., De Rochefort, L., et al: Morphology enabled dipole inversion (MEDI) from a single-angle acquisition: comparison with COSMOS in human brain imaging. *Magnetic Resonance in Medicine* **66**(3), 777–783 (2011)
18. Liu, T., Spincemaille, P., De Rochefort, L., et al: Calculation of susceptibility through multiple orientation sampling (COSMOS): a method for conditioning the inverse problem from measured magnetic field map to susceptibility source image in MRI. *Magnetic Resonance in Medicine* **61**(1), 196–204 (2009)
19. Liu, T., Wisnieff, C., Lou, M., et al: Nonlinear formulation of the magnetic field to source relationship for robust quantitative susceptibility mapping. *Magnetic Resonance in Medicine* **69**(2), 467–476 (2013)

20. Marques, J., Bowtell, R.: Application of a Fourier-based method for rapid calculation of field inhomogeneity due to spatial variation of magnetic susceptibility. *Concepts in Magnetic Resonance Part B: Magnetic Resonance Engineering* **25**(1), 65–78 (2005)
21. Milovic, C., Bilgic, B., Zhao, B., et al: Fast nonlinear susceptibility inversion with variational regularization. *Magnetic Resonance in Medicine* **80**(2), 814–821 (2018)
22. Odena, A., Dumoulin, V., Olah, C.: Deconvolution and checkerboard artifacts. *Distill* **1**(10), e3 (2016)
23. Polak, D., Chatnuntawech, I., Yoon, J., et al: Nonlinear dipole inversion (NDI) enables robust quantitative susceptibility mapping (QSM). *NMR in Biomedicine* p. e4271 (2020)
24. de Rochefort, L., Liu, T., Kressler, B., et al: Quantitative susceptibility map reconstruction from MR phase data using bayesian regularization: validation and application to brain imaging. *Magnetic Resonance in Medicine* **63**(1), 194–206 (2010)
25. Salomir, R., de Senneville, B.D., Moonen, C.T.: A fast calculation method for magnetic field inhomogeneity due to an arbitrary distribution of bulk susceptibility. *Concepts in Magnetic Resonance Part B: Magnetic Resonance Engineering* **19**(1), 26–34 (2003)
26. Schweser, F., Zivadinov, R.: Quantitative susceptibility mapping (QSM) with an extended physical model for MRI frequency contrast in the brain: a proof-of-concept of quantitative susceptibility and residual (QUASAR) mapping. *NMR in Biomedicine* **31**(12), e3999 (2018)
27. Shmueli, K., de Zwart, J.A., van Gelderen, P., et al: Magnetic susceptibility mapping of brain tissue in vivo using MRI phase data. *Magnetic Resonance in Medicine* **62**(6), 1510–1522 (2009)
28. Smith, S.M.: Fast robust automated brain extraction. *Human Brain Mapping* **17**(3), 143–155 (2002)
29. Uecker, M., Lai, P., Murphy, M.J., et al: ESPIRiTan eigenvalue approach to autocalibrating parallel mri: where sense meets GRAPPA. *Magnetic Resonance in Medicine* **71**(3), 990–1001 (2014)
30. Ulyanov, D., Vedaldi, A., Lempitsky, V.: Deep image prior. In: *Proceedings of the IEEE CVPR*. pp. 9446–9454 (2018)
31. Wang, Y., Liu, T.: Quantitative susceptibility mapping (QSM): decoding MRI data for a tissue magnetic biomarker. *Magnetic Resonance in Medicine* **73**(1), 82–101 (2015)
32. Wharton, S., Schäfer, A., Bowtell, R.: Susceptibility mapping in the human brain using threshold-based k-space division. *Magnetic Resonance in Medicine* **63**(5), 1292–1304 (2010)
33. Wu, B., Li, W., Guidon, A., Liu, C.: Whole brain susceptibility mapping using compressed sensing. *Magnetic Resonance in Medicine* **67**(1), 137–147 (2012)
34. Yoon, J., Gong, E., Chatnuntawech, I., et al: Quantitative susceptibility mapping using deep neural network: QSMnet. *NeuroImage* (2018)